Open-orbit theory of photoionization microscopy on nonhydrogenic atoms

F. L. Liu[1,2] and L. B. Zhao[2,*]

[1]*College of Physical Sciences and Technology, Heilongjiang University, Harbin 150080, China*

[2]*Atomic and Molecular Physics Division, Center for Analysis and Testing, Harbin Normal University, Harbin 150025, China*

(Received 24 January 2017; published 27 April 2017)

Semiclassical open-orbit theory (OOT), previously developed to study photoionization of hydrogenic atoms in a uniform electric field [L. B. Zhao and J. B. Delos, Phys. Rev. A **81**, 053417 (2010)], has been generalized to describe the propagation of outgoing electron waves to macroscopic distances from a nonhydrogenic atomic source. The generalized OOT has been applied to calculate spatial distributions of electron probability densities and current densities, produced due to photoionization for lithium in a uniform electric field. The obtained results are compared with those from the fully quantum-mechanical coupled-channel theory (CCT). The excellent agreement between the CCT and OOT confirms the reliability of the generalized OOT. Comparison is also made with theoretical calculations from the wave-packet propagation technique and the recent photoionization microscopy experiment. The existing difference between theory and experiment is discussed.

DOI: 10.1103/PhysRevA.95.043428

I. INTRODUCTION

Imaging electronic wave functions (or more strictly, imaging probability densities of wave functions) of single atoms and molecules has attracted researchers' attention for decades because of fundamental physics interest in quantum systems themselves and its importance in many applications. The development of ultrafast techniques makes it possible to experimentally observe single molecular orbitals on the timescale of chemical reaction [1]. Recently, tomographic reconstruction of the highest occupied molecular orbitals of N_2 has been implemented [2]. Apparently, such an investigation is crucial to understanding the essence of chemistry as well as controlling chemical reaction. Subsequently, the tomography approach developed has been extended to measure atomic wave functions of He and Ne, and symmetries of the probed atomic wave functions are resolved by manipulating the electron-ion recollision [3].

Besides the ultrafast techniques, another kind of imaging techniques called photoionization microscopy has also been established to visualize wave functions of single atoms and molecules on a macroscopic scale [4]. Although the concept of photoionization microscopy was first introduced by Nicole *et al.* [4], the crucial idea of this concept was proposed in the early 1980s by Fabrikant [5] and Demkov *et al.* [6], who suggested that slow photoelectron currents, produced due to photoionization of atoms in the presence of a uniform static electric field, are recorded on a position-sensitive two-dimensional detector located at a macroscopic distance, while the squared moduli of the wave functions are extracted from the photoelectron signal recorded. They derived the expressions of differential cross sections and predicted the oscillatory structures of the outgoing wave functions. Subsequently, a series of theoretical studies on photoionization microscopy of hydrogenic atoms was reported in the 1980s and early 1990s, based on semiclassical theory [7].

The observation of slow photoelectron imaging was first implemented by Nicole *et al.* [8], and a classical and a quantum-mechanical calculation were also presented to interpret the observed images. It was found that the outer and inner rings exhibited in the images are caused by the indirect and direct ionization process, respectively. Their investigation reveals that the indirect process dominates for lower energies close to the saddle point, whereas the direct one dominates for higher energies close to the field-free ionization threshold. The slow photoelectron imaging setup was subsequently developed into the velocity map imaging apparatus by the same group [4], and using the apparatus, the electron currents for Xe from its metastable state $6s[3/2]_2$ placed in a uniform electric field of 320 V/cm were measured and compared to those from semiclassical theory. The comparison shows qualitative agreement. A detailed semiclassical analysis was published by Bordas *et al.* [9] following the Xe measurement.

A semiclassical open-orbit theory (OOT) for hydrogenic atoms has recently been developed to describe the electron wave propagation in the combined Coulomb and electric fields [10]. In contrast with the semiclassical formulation of Bordas *et al.* [9], in which Maslov indices are not included, tunneling into classically forbidden regions is not treated, and singularities at caustics are not corrected, the OOT incorporates all three effects. The OOT has been applied to calculations of photoionization microscopy. The photoelectron current densities were predicted for H atoms in an electric field of 5714 V/cm using the OOT and the obtained images were found to be in excellent agreement with those from the completely quantum-mechanical calculations [11]. The comparison has confirmed the reliability of the OOT.

The technique progress of photoionization microscopy makes it possible to visualize electron standing wave tunneling through the potential barrier formed by the superposition of the Coulomb and electric fields. Very recently, the wave-function microscopy images on Stark resonances were observed for Li atoms by Cohen *et al.* [12] and H atoms by Stodolna *et al.* [13]. These images were found to clearly display signatures of quasi-bound electronic states. The time-dependent calculations from the wave-packet propagation technique were also presented. The theoretical and experimental results were compared, but only qualitative agreement is seen for both H and Li atoms. A simulation of wave-function microscopy images on Stark

*Corresponding author: libo.zhao@hrbnu.edu.cn

resonances was performed to explain the existing differences for H atoms using the quantum-mechanical formulation [14]

Following their previous work in their Letter [12], Cohen *et al.* [15] published a more detailed experimental study on photoionization microscopy for Li atoms, accompanying a time-dependent calculation from the wave-packet propagation technique. The wave-function imaging for quasibound resonance and continuum Stark states was reported. A general description was presented for photoionization microscopy of Li atoms with emphasis on the various manifestations of resonant characters. The experimental images are qualitatively explained by the theoretical calculations. Their analysis concluded that resonance effects are easily identified for H atoms, but hardly identified for heavy atoms like Xe atoms. The Li atom is regarded as a better example for showing quasibound resonance states between the two limiting cases, the light and heavy atoms.

The semiclassical OOT [10] was developed to describe the propagation of outgoing electron waves due to photoionization of hydrogenic atoms in the presence of an external electric field, and hence invalid for nonhydrogenic atoms. In this paper, we generalize the OOT to deal with photoionization of Stark nonhydrogenic atoms. The effects of atomic cores are incorporated in the generalized OOT, and the electron wave propagation to a macroscopic distance from a nonhydrogenic atomic source is formulated. It has been shown in Ref. [10] that the OOT provides a clear and intuitive physical picture to help understand the physical origin of structures in the electron current distribution. For example, the structures of observed geometrical interference patterns on the detector may be due to direct or indirect ionization processes. These structures are intuitively comprehensible in terms of the OOT.

The manuscript is organized as follows. Section II is devoted to the development of the generalized open-orbit theory, describing the electron wave propagation in the space from a nonhydrogenic atomic source in the presence of an external electric field. First we give a general description of the generalized OOT beginning from dividing the configuration space into the inner and outer regions. The expression of field-free outgoing electron waves in the Coulomb region is derived, and the main formulas for wave propagation in the outer region is outlined in this section. We also sketch the solution of the classical equations of motion for completeness of theory. In Sec. III, the developed generalized OOT is applied to calculations of photoionization of Stark Li atoms. The spatial distributions of electron probability densities and current densities are predicted for photoionization of the ground-state Li atoms. Comparison with the other theoretical results and the recent photoionization microscopy experiment is performed. The influence of atomic cores on the spatial distributions of electron probability densities is discussed. Section IV summarizes the generalized OOT of photoionization microscopy and our main conclusions. Atomic units are used throughout this paper unless otherwise noted.

II. OPEN-ORBIT THEORY FOR NONHYDROGENIC ATOMS

Let us consider an atom in the initial state placed in a uniform electric field. When such an atom is irradiated by a laser beam, it may absorb a photon and then may be excited to different field-free Rydberg states, dependent on laser frequency. It is well known that there do not exist bound states theoretically for atoms in external electric fields, and they are *in principle* in ionization states. This ionization process produces steady outgoing electron waves. The propagation of the outgoing electron waves to macroscopic distance from a hydrogenic atom source has been formulated by Zhao and Delos [10]. Here we concentrate on the electron wave propagation from a nonhydrogenic atom source.

First we divide the configuration space of nonhydrogenic atoms in an external electric field into the inner and outer regions, and assume that effects of external fields on the atomic systems in the inner region are negligible. Thus we can use field-free quantum-mechanical methods to calculate wave functions for multielectronic atoms in the inner region. We further divide the inner region into the short-range interaction region and Coulomb region. The field-free quantum-mechanical theory for multielectronic atoms explicitly shows that all the complex dynamics describing the electron-electron interaction occurs in a small short-range region near the nucleus, while the active electron feels only the Coulomb potential in the Coulomb region. Based on this scheme to divide the configuration space, the wave functions in the Coulomb region can be written as a linear combination of regular and irregular Coulomb wave solutions. When the active electron moves in the outer region, it feels only the Coulomb potential and the external electric field. We assume that the electron moves in this region following classical trajectories, and semiclassical wave functions associated with these classical trajectories are constructed by solving the classical equations of motion.

A. Electron wave propagation from the atomic source to the Coulomb region

After atoms in the initial state placed in a uniform electric field absorb photons, outgoing electron waves are produced and propagate forward from the atomic source to the Coulomb region, where influence of the external electric field on the atomic systems is so small that it is negligible. In this section, we formulate the outgoing electron wave functions in the inner region. Let us consider alkali-metal atoms with a closed core and a valence electron in highly excited states. The complicated dynamics of alkali-metal atoms may be substantially simplified to the motion of the highly excited Rydberg electron in the Coulomb potential plus a short-range spherically symmetric core potential. Here we denote the potential for the atomic system with $V(r)$ satisfying boundary conditions $V(r) \xrightarrow{r\to 0} -Z/r$ and $V(r) \xrightarrow{r\to\infty} -1/r$, where Z is the atomic number.

To derive the expression for outgoing wave functions in the Coulomb region, we begin from the inhomogeneous Schrödinger equation,

$$(E - \widehat{H})\psi_{\rm out}(\boldsymbol{r}) = D\psi_{\rm ini}(\boldsymbol{r}), \tag{1}$$

where $\psi_{\rm out}(\boldsymbol{r})$ represents the outgoing wave function, D is the dipole operator, $\psi_{\rm ini}(\boldsymbol{r})$ is the wave function for the initial bound state of the system, and $D\psi_{\rm ini}(\boldsymbol{r})$ denotes the source term describing the interaction between the atom and radiation

field. The solution $\psi_{\rm out}(\boldsymbol{r})$ can be expressed as Green's function $G(\boldsymbol{r},\boldsymbol{r'})$, acting upon the source,

$$\psi_{\rm out}(\boldsymbol{r}) = \int G(\boldsymbol{r},\boldsymbol{r'}) D\psi_{\rm ini}(\boldsymbol{r'}) d\boldsymbol{r'}, \tag{2}$$

where Green's function satisfies

$$\left[E - \left(-\tfrac{1}{2}\nabla^2 + V(r)\right)\right] G(\boldsymbol{r},\boldsymbol{r'}) = \delta(\boldsymbol{r} - \boldsymbol{r'}). \tag{3}$$

The expansion of the three-dimensional Green's function $G(\boldsymbol{r},\boldsymbol{r'})$ in spherical harmonics is

$$G(\boldsymbol{r},\boldsymbol{r'}) = \sum_{\ell,m} Y^*_{\ell m}(\theta',\phi') \mathrm{g}_\ell(r,r') Y_{\ell m}(\theta,\phi), \tag{4}$$

where $\mathrm{g}_\ell(r,r')$ denotes the radial Green's function. Its expression will be derived below.

The delta function $\delta(\boldsymbol{r} - \boldsymbol{r'})$ in spherical coordinates is written as

$$\delta(\boldsymbol{r} - \boldsymbol{r'}) = \frac{1}{r'^2 \sin\theta'} \delta(r - r')\delta(\theta - \theta')\delta(\phi - \phi'). \tag{5}$$

Inserting the above equation and Eq. (4) into Eq. (3) produces

$$\begin{aligned} &\left[\frac{1}{r^2}\frac{\partial}{\partial r}\left(r^2\frac{\partial}{\partial r}\right) - \frac{\hat{\ell}^2}{r^2} + 2[E - V(r)]\right] \\ &\quad \times \sum_{\ell,m} Y^*_{\ell m}(\theta',\phi') \mathrm{g}_\ell(r,r') Y_{\ell m}(\theta,\phi) \\ &= \frac{2}{r'^2 \sin\theta'} \delta(r - r')\delta(\theta - \theta')\delta(\phi - \phi'). \end{aligned} \tag{6}$$

Multiplying the two sides of the above equation by $Y_{\overline{\ell},\overline{m}}(\theta',\phi') \sin\theta'$ and integrating over θ', ϕ', we have

$$\begin{aligned} &\left[\frac{1}{r^2}\frac{\partial}{\partial r}\left(r^2\frac{\partial}{\partial r}\right) - \frac{\ell(\ell+1)}{r^2} + 2[E - V(r)]\right] \mathrm{g}_\ell(r,r') \\ &= \frac{2}{r'^2}\delta(r - r'), \end{aligned} \tag{7}$$

where the overlines of $\overline{\ell}$ and $\overline{m}$ in Eq. (7) are removed after the operation. Apparently, doing so does not affect the equation.

Defining the modified radial Green's function

$$\frac{\overline{\mathrm{g}}_\ell(r,r')}{rr'} = \mathrm{g}_\ell(r,r'), \tag{8}$$

and substituting it into Eq. (7), one obtains the inhomogeneous differential equation,

$$\left[\frac{d^2}{dr^2} - \frac{\ell(\ell+1)}{r^2} + 2[E - V(r)]\right] \overline{\mathrm{g}}_\ell(r,r') = 2\delta(r - r'). \tag{9}$$

It is easily seen that the solution of the equation is continuous, but its derivative suffers a discontinuity at $r = r'$. Direct integration of Eq. (9) with respect to r from $r - \epsilon$ to $r + \epsilon$ yields the discontinuity

$$\lim_{\epsilon\to 0} \left.\frac{d\overline{\mathrm{g}}_\ell(r,r')}{dr}\right|_{r=r'-\epsilon}^{r=r'+\epsilon} = 2. \tag{10}$$

The property of the discontinuity of the derivative of $\overline{\mathrm{g}}_\ell$ given above will be used later.

To obtain the expression of the radial Green's function, we resort to the boundary conditions that $\overline{\mathrm{g}}_\ell$ satisfies. The boundary conditions require that the modified radial Green's function $\overline{\mathrm{g}}_\ell(r,r')$ behaves as [16]

$$\overline{\mathrm{g}}_\ell(r,r') \sim \begin{cases} \mathcal{F}_{\mathrm{sw}\ell}(r), & r \to 0, \\ \mathcal{F}^{\rm out}_\ell(r), & r \to \infty, \end{cases} \tag{11}$$

where $\mathcal{F}_{\mathrm{sw}\ell}$ denotes the standing-wave solution for the radial Schrödinger equation for alkali-metal atoms without a source, a homogenous Schrödinger equation, and $\mathcal{F}^{\rm out}_\ell$ is the outgoing wave solutions. $\mathcal{F}_{\mathrm{sw}\ell}$ in the Coulomb region can be written as

$$\mathcal{F}_{\mathrm{sw}\ell}(r) = s_\ell(r) + c_\ell(r)\tan\pi\mu_\ell, \tag{12}$$

where s_ℓ and c_ℓ represent the regular and irregular Coulomb function, respectively, and μ_ℓ is the quantum defect for the ℓ partial wave. s_ℓ and c_ℓ with zero energy are of the asymptotic form

$$s_\ell(r) = \left(\frac{2r}{\pi^2}\right)^{1/4} \sin(\sqrt{8r} - \ell\pi - \pi/4), \tag{13}$$

$$c_\ell(r) = \left(\frac{2r}{\pi^2}\right)^{1/4} \cos(\sqrt{8r} - \ell\pi - \pi/4), \tag{14}$$

while the asymptotic form of the outgoing wave $\mathcal{F}^{\rm out}_\ell$ is written as

$$\mathcal{F}^{\rm out}_\ell(r) = c_\ell(r) + i s_\ell(r) = \left(\frac{2r}{\pi^2}\right)^{1/4} e^{i(\sqrt{8r} - \ell\pi - \pi/4)}. \tag{15}$$

Except in the vicinity of $r = r'$, the modified radial Green's function must satisfy the homogenous differential equation. This further implies that the form of the modified radial Green's function should be written as

$$\overline{\mathrm{g}}_\ell(r,r') = \begin{cases} C\mathcal{F}_{\mathrm{sw}\ell}(r)\mathcal{F}^{\rm out}_\ell(r'), & r \leqslant r', \\ C\mathcal{F}^{\rm out}_\ell(r)\mathcal{F}_{\mathrm{sw}\ell}(r'), & r \geqslant r', \end{cases} \tag{16}$$

where C is the constant that is determined by the discontinuity of the derivative of $\overline{\mathrm{g}}_\ell(r,r')$ at $r = r'$. Inserting Eq. (16) into Eq. (10) produces $-CW = 2$, where W is the Wronskian for $\mathcal{F}_{\mathrm{sw}\ell}(r)$ and $\mathcal{F}^{\rm out}_\ell(r)$. Following Seaton [17], it is readily shown that $C = \pi/(1 - i\tan\pi\mu_\ell)$. The modified radial Green's function is finally written as

$$\overline{\mathrm{g}}_\ell(r,r') = \pi i [\mathcal{F}^-_\ell(r_<)]^* \mathcal{F}^{\rm out}_\ell(r_>), \tag{17}$$

with

$$\mathcal{F}^-_\ell(r_<) = i\mathcal{F}_{\mathrm{sw}\ell}(r_<)(1 + iK)^{-1}, \tag{18}$$

where $r_< = \min(r,r')$, $r_> = \max(r,r')$, and $K = \tan\pi\mu_\ell$ represents the reaction matrix.

Thus $\mathrm{g}_\ell(r,r')$ can be written as

$$\mathrm{g}_\ell(r,r') = \pi i [R^-_\ell(r_<)]^* R^{\rm out}_\ell(r_>), \tag{19}$$

with $R^-_\ell(r_<) = \mathcal{F}^-_\ell(r_<)/r_<$ and $R^{\rm out}_\ell(r_>) = \mathcal{F}^{\rm out}_\ell(r_>)/r_>$. Inserting the expression for the radial Green's function, Eq. (19), into Eq. (4), one obtains the three-dimensional Green's function, and as a consequence the outgoing wave function is finally written as

$$\psi_{\rm out}(\boldsymbol{r}) = \pi i \sum_{\ell,m} R^{\rm out}_\ell(r) Y_{\ell m}(\theta,\phi) \mathcal{D}_\ell, \tag{20}$$

with $\mathcal{D}_\ell$ being the dipole transition matrix element

$$\mathcal{D}_\ell = \int [R_\ell^-(r')Y_{\ell m}(\theta',\phi')]^* D\psi_{\rm ini}(\boldsymbol{r}')d\boldsymbol{r}'. \quad (21)$$

For atomic systems with energies $E = 0$, from Eq. (15) the outgoing wave function $R_\ell^{\rm out}$ turns out to be

$$R_\ell^{\rm out}(r) = \left(\frac{2}{\pi^2 r^3}\right)^{1/4} e^{i(\sqrt{8r}-\ell\pi-\pi/4)}. \quad (22)$$

One may utilize Eq. (22) to approximate the outgoing wave functions if the ionized electrons are of energies close to zero. Du and Delos [18] have shown that such an approximation makes an error to be negligibly small. Substituting Eq. (22) into Eq. (20) yields

$$\psi_{\rm out}(\boldsymbol{r}) = i\pi^{1/2}2^{1/4}e^{-i\pi/4}\sum_m \frac{\exp(i\sqrt{8r})}{r^{3/4}}\mathcal{Y}_m(\theta)e^{im\phi}, \quad (23)$$

with

$$\mathcal{Y}_m(\theta) = \sum_\ell (-1)^\ell Y_{\ell m}(\theta,0)\mathcal{D}_\ell. \quad (24)$$

We would point out that in the present paper we utilize the solution of outgoing waves at infinity to represent the outgoing wave in the intermediate (Coulomb) region. Generally this is an approximation since this approach does not include rescattering and the above-barrier reflection. A detailed discussion on this topic has been given in Ref. [19]. It is discovered that if the energy is well above the saddle point, this approximation is valid; but for energies close to the saddle point there will be significant discrepancies.

It should be emphasized that Gao and Delos [20] give the expression of outgoing wave functions for alkali-metal atoms to calculate photoabsorption spectra for alkali-metal atoms in an external electric field, within the framework of closed-orbit theory developed by Du and Delos [18]. However, Gao and Delos do not give the detailed derivation. Their derivation begins from constructing the solutions for the radial Schrödinger equation in the Coulomb region, but lacks the necessary theoretical steps for the complete understanding of this dynamics process including both the short-range interaction region and Coulomb region. Even so, it can be proven that their expression is consistent with ours at $E = 0$ except for a phase shift π. Our expression of outgoing wave functions is valid for $E \geqslant 0$ and therefore is more general.

B. Semiclassical propagation of electron waves from the Coulomb region to macroscopic distances

When the outgoing electron waves propagate to the Coulomb region, influence of the external electric field on the atomic systems begins to become important. From the Coulomb region to macroscopic distances, these waves propagate outward in the combined Coulomb and electric fields. We adopt the semiclassical approximation to describe the wave propagation in the outer region, and take a spherical surface with a spherical radius $r_0 = 10a_0$–$100a_0$ to divide the configuration space into the inner and outer regions. On the spherical surface, the field-free outgoing wave functions are calculated using Eq. (23). The final result for the outgoing waves should be independent of the choice of r_0, once it is reasonably taken. This will be examined in detail in the later calculations.

Consider an ionized electron from the atomic source. We denote the three-dimensional coordinates of the electron on the detector with $\boldsymbol{q}$, and on the initial surface with $\boldsymbol{q}_0$. Suppose that the electron wave begins to propagate outward at time t_0 from the initial surface and arrives at the detector at time t. The outgoing wave given by Eq. (23) is joined to the semiclassical wave on the initial surface. The semiclassical wave function in the outer region is of the form

$$\Psi(\boldsymbol{q}) = \sum_j \psi_{\rm out}^j(\boldsymbol{q}_0)A_j(\boldsymbol{q})e^{i[S_j(\boldsymbol{q})-\mu_j\pi/2]}, \quad (25)$$

with

$$S_j(\boldsymbol{q}) = \int_{\boldsymbol{q}_0}^{\boldsymbol{q}} \boldsymbol{p}\cdot d\boldsymbol{q}, \quad (26)$$

$$A_j(\boldsymbol{q}) = [J(t_0,\boldsymbol{q}_0)/J(t,\boldsymbol{q})]^{1/2}, \quad (27)$$

where $S_j(\boldsymbol{q})$ is the classical action on the jth trajectory, $A_j(\boldsymbol{q})$ is the classical amplitude on the jth trajectory, μ_j is the Maslov index for the jth trajectory, and J is a three-dimensional Jacobian defined in Ref. [10]. The summation in Eq. (25) runs over all trajectories that begin from different points $\boldsymbol{q}_0$ on the initial spherical surface and arrive at a given point $\boldsymbol{q}$.

C. Solutions of the classical equations of motion

The open-orbit theory for hydrogenic atoms in an electric field has been published in Ref. [10], and its theoretical and computational details can be found there. Here we only outline the solutions of the classical equation of motion for the electron in the combined Coulomb and electric fields, and search for classical trajectories that can arrive at a given point $\boldsymbol{q}$ on the detector. Such trajectories are defined as *open orbits* by Zhao and Delos [10]. The electrons traveling along open orbits can escape from the atoms and propagate to a large distance. In contrast with open orbits, those trajectories that never escape from the atoms are defined as *bound orbits*. Also we sketch calculations of the classical outgoing wave functions as follows.

In the semiparabolic coordinates $u = \sqrt{r+z}$, $v = \sqrt{r-z}$ and $\phi = \tan^{-1}(y/x)$, the effective Hamiltonian of hydrogen atoms in an external electric field $\mathscr{F}$ in atomic units is written in the form [10]

$$\mathscr{H} = \frac{1}{2}(p_u^2 + p_v^2) + \frac{\mathscr{L}_z^2}{2u^2} + \frac{\mathscr{L}_z^2}{2v^2} - 2 + \frac{1}{2}(u^4 - v^4) - \epsilon(u^2+v^2), \quad (28)$$

where $\epsilon = E/\mathscr{F}^{1/2}$, and $\mathscr{L}_z = m\hbar\mathscr{F}^{1/4}$ is the z component of the scaled effective angular momenta. From the effective Hamiltonian, the classical equations of motion are readily obtained. Differentiating the obtained equations of motion with respect to the emission angle of electrons θ yields four additional equations:

$$\frac{d}{d\tau}\left(\frac{\partial u}{\partial\theta}\right) = \frac{\partial p_u}{\partial\theta}, \quad (29)$$

$$\frac{d}{d\tau}\left(\frac{\partial v}{\partial\theta}\right)=\frac{\partial p_v}{\partial\theta}, \tag{30}$$

$$\frac{d}{d\tau}\left(\frac{\partial p_u}{\partial\theta}\right)=\left(-3\frac{\mathscr{L}_z^2}{u^3}+2\epsilon-6u^2\right)\frac{\partial u}{\partial\theta}, \tag{31}$$

$$\frac{d}{d\tau}\left(\frac{\partial p_v}{\partial\theta}\right)=\left(-3\frac{\mathscr{L}_z^2}{v^3}+2\epsilon+6v^2\right)\frac{\partial v}{\partial\theta}, \tag{32}$$

where the independent variable τ is the "fictitious time" defined in Ref. [10]. These four additional equations are solved together with the equations of motion for convenience of the Jacobian calculations.

It is shown in the previous analysis [10] that not any trajectories can travel for a large distance. Only so-called open orbits, which are of emission angles larger than the critical angle $\theta_c = 2\sin^{-1}(-E/2\sqrt{\mathscr{F}})$, can escape from the Coulomb-Stark potential and reach the detector. Let the detector be fixed at a given value, and then we integrate the equations of motion and Eqs. (29)–(32). Once a trajectory reaches the detector, its cylindrical coordinate $\rho_f(\theta_i)$ is recorded, and a graph of ρ_f as a function of $\log_{10}(\theta_i-\theta_c)$ is plotted. After that, the obtained curve is divided into segments, with each segment connecting a zero to an extremum. In each segment, we use a Newton root-finding algorithm to search for trajectories to hit a given point on the detector. Although in principle an infinite number of trajectories can arrive at a given point, it is discovered that the amplitudes associated with these trajectories decrease quickly, and only the limited trajectories make a non-negligible contribution to the interference pattern on the detector.

After all open orbits to hit a given point on the detector are found, the associated actions, three-dimensional Jacobians, and classical amplitudes are calculated from the solutions of the equations of motion. The Maslov indices, which are crucial to the exact determination of the interference pattern, are also counted along each trajectory. Finally, the outgoing electron wave functions are obtained from Eq. (25).

D. Probability density and electron current density

To compare with experimental wave-function microscopy images, it is essential to calculate the spatial distribution of probability densities and electron current densities. Their formulas have been given in Ref. [10]. Here they are listed for convenience of readers. Let the detector be perpendicular to the z axis. In cylindrical coordinates (ρ, z, φ), the probability density is

$$\mathcal{P}(\rho,z_{\rm det},\varphi)=|\Psi(\rho,z_{\rm det},\varphi)|^2 \tag{33}$$

and the probability density integrated over an azimuthal angle φ is

$$\mathcal{P}(\rho,z_{\rm det})=\int_0^{2\pi}|\Psi(\rho,z_{\rm det},\varphi)|^2\rho d\varphi. \tag{34}$$

The electron current density, or the differential cross section, is determined by [21]

$$\frac{d\sigma(\boldsymbol{r})}{ds}=\frac{2\pi\omega}{c}\boldsymbol{j}\cdot\boldsymbol{n}, \tag{35}$$

where ω is the photon frequency, c is the speed of light, $\boldsymbol{n}$ is a unit vector normal to the screen at $\boldsymbol{r}$, and $\boldsymbol{j}$ is defined by

$$\boldsymbol{j}=\frac{i}{2}[\Psi^*(\boldsymbol{r})\nabla\Psi(\boldsymbol{r})-\Psi(\boldsymbol{r})\nabla\Psi^*(\boldsymbol{r})]. \tag{36}$$

III. RESULTS AND DISCUSSION

Using the generalized open-orbit theory characterized in the preceding sections, we calculated spatial distributions of electron probability densities and current densities produced by photoionization for ground-state Li atoms in a uniform electric field. Let us consider Li atoms in an electric field ionized by a beam of laser light of tunable frequency. The laser is assumed to be linearly polarized with polarization parallel to the electric field. The field-free dipole matrix elements for transitions from an initial state to a final state are calculated using wave functions obtained by solving the Schrödinger equation. A model potential for Li atoms is adopted to describe the interaction between the residual ion and the outer valence electron [22]. This model potential has been found to produce wave functions for initial and final states, and quantum defects to be sufficiently exact [23]. Even so, one should be careful when a model potential is utilized for the other atoms. It has been shown that for some atoms, a pseudopotential may be better than a model potential [24]. This is because in contrast to the model potential, the pseudopotential incorporates the Pauli exclusion principle, and therefore an active electron is prevented from the transition to lower states occupied by inner electrons.

To test the reliability of the generalized OOT, we calculated spatial distributions of electron probability densities for Stark Li atoms. The obtained results are compared to those from the fully quantum-mechanical coupled-channel theory [23]. Figure 1 illustrated the integrated probability densities at the field strength 1000 V/cm for two energies away from any resonance from both the generalized OOT and CCT. Excellent agreement between the two theories can be seen in this figure. We took a large number of energies above the saddle point and field strengths from 615 to 5714 V/cm, and agreement of the two theories for all the energies and field strengths taken illustrates that the generalized OOT can produce sufficiently exact probability densities. For Li atoms, we checked the effect of scattering from closed orbits to open orbits on spatial distributions of electron probability densities. The scattering from a closed orbit to another closed orbit has been treated by Gao *et al.* [20,25]. Here we generalized their scheme to consider scattering from a closed orbit to an open orbit and found that the contribution of such scattering to spatial distributions of electron probability densities is negligibly small.

The integrated probability densities for Stark H and ground-state Li atoms are compared in Fig. 2. It is assumed that the initial state for H atoms is $\psi_{\rm ini}(\boldsymbol{r})=\frac{1}{\sqrt{2}}[\psi_{2s}(\boldsymbol{r})-\psi_{2p}(\boldsymbol{r})]$, with $m=0$. It is well known that the uniform electric field couples the $2s$ and $2p$ states, where $\psi_{2s}(\boldsymbol{r})$ and $\psi_{2p}(\boldsymbol{r})$ indicate wave functions for field-free H atoms. The figure displays the pronounced discrepancy between H and Li results. Such a discrepancy illustrates the significant effect of atomic cores on probability density distributions for ejected electrons.

The nature of classical trajectories for Stark H atoms was first emphasized by Bordas *et al.* [9,26]. They divide these trajectories into direct and indirect parts, and illustrate that the direct trajectories are those that never intersect the z axis, while the indirect trajectories intersect the z axis at least once. Here the generalized OOT is utilized to investigate the contribution from the direct and indirect trajectories to the interference pattern for Stark Li atoms. Figure 3 gives the radial distributions of electron current densities for Li atoms at a field strength of 1000 V/cm for six energies, which are higher than an energy threshold $E_{\rm dir} = \kappa E_{\rm sp}$ corresponding to the onset of direct trajectories, where $E_{\rm sp}$ represents the saddle-point energy, and $\kappa \approx -0.776156$ given by Bordas *et al.* [9]. This figure displays the evolution of the electron current densities with energies. The contour plots accompanying each photoelectron image are illustrated in

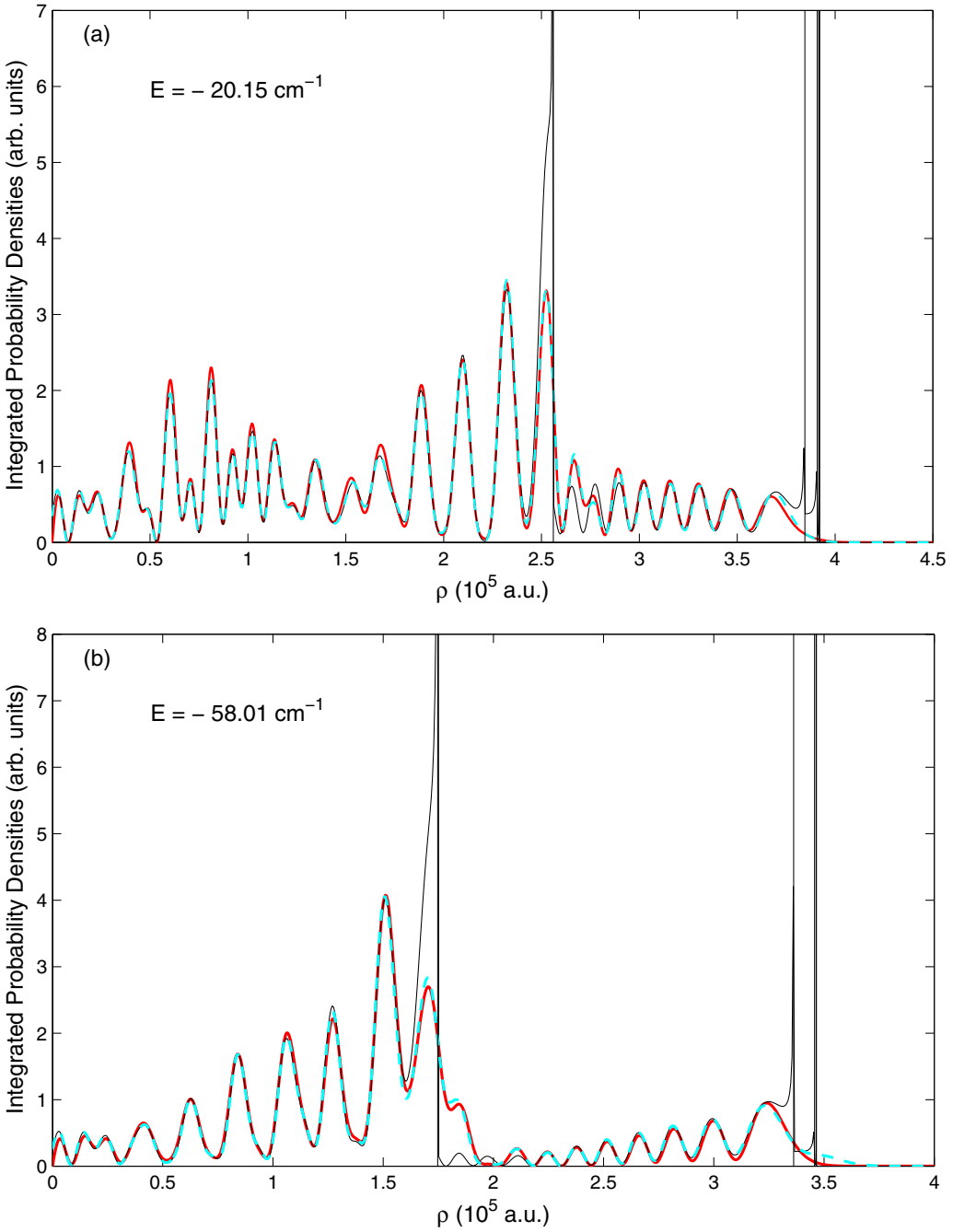

FIG. 1. Radial distribution of probability densities, integrated over the angular variable φ of cylindrical coordinates (ρ, z, φ) of the ejected photoelectron at two energies, -20.15 and -58.01 cm^{-1}. Li atoms are placed in a uniform electric field with strength 1000 V/cm, and the detector is located at $z_{\rm det} = -1000$ μm from the origin. The black curves represent the results from the generalized OOT, which gives divergent probability densities at caustics denoted with the black vertical lines, and the cyan dashed curves indicate those from the uniform approximation. The red curves are from the fully quantum-mechanical CCT. Excellent agreement between CCT and OOT confirms the reliability of the generalized OOT developed in the present work.

Fig. 4. Our calculations show that the contribution of direct trajectories to the interference pattern on a detector appears only between the origin and the first caustic surface for each energy from -114.59 to -21.873 cm^{-1}. In particular, one sees from the graph at -114.59 cm^{-1} that the direct trajectories preponderantly contribute to the interference pattern. This conclusion is consistent with that of Cohen *et al.* [15]. Their experiment shows that the indirect contribution to the interference pattern on a detector is quite faint and hardly observable for a number of images with E close to $E_{\rm dir}$.

Figure 3 exhibits that the distances from the origin to the first caustic surfaces become larger and larger with increasing E. This illustrates the effect of the direct trajectories on the interference pattern. We simulated the photoelectron images for each energy as given in Fig. 3 by removing the contribution from the direct trajectories and found that the direct trajectories play a dominant role in photoionization of Li atoms in a uniform electric field. Such a result is consistent with the theoretical prediction made by Bordas *et al.* [9,26] as well as the experimental results of Cohen *et al.* [15].

The spatial distributions of electron current densities for Li atoms are simulated at a field strength of 1000 V/cm for four energies, -179.54, -180.45, -182.70, and -185.18 cm^{-1} using the generalized OOT. The obtained results are compared

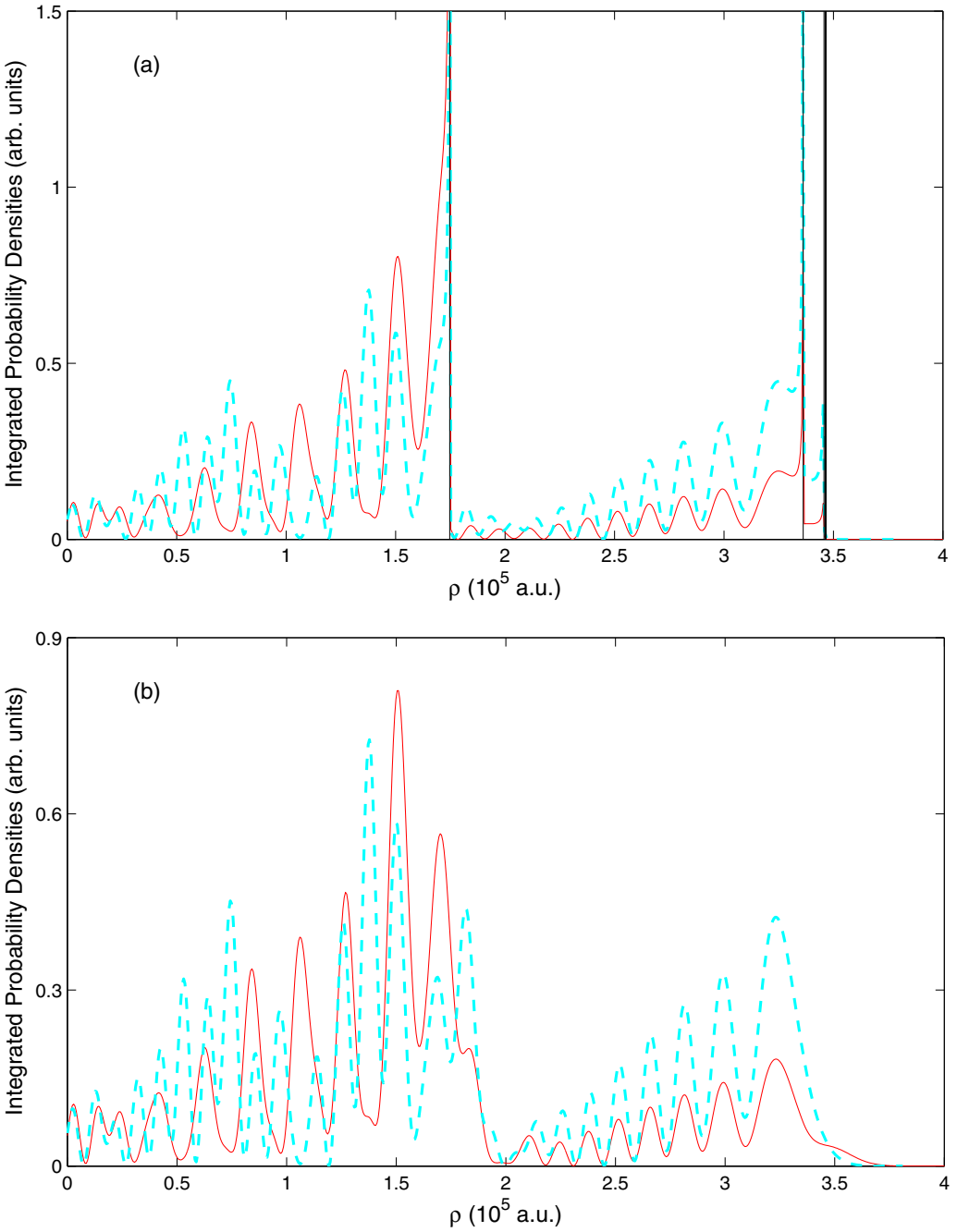

FIG. 2. Comparison of the integrated probability densities for Li and H atoms at -58.01 cm^{-1}. (a) Semiclassical results; (b) the uniform approximation. The field strength is 1000 V/cm and the detector is located at $z_{\rm det} = -1000$ μm from the atomic origin. The red solid and cyan dashed curves represent Li and H results, respectively, and the black vertical lines denote caustics.

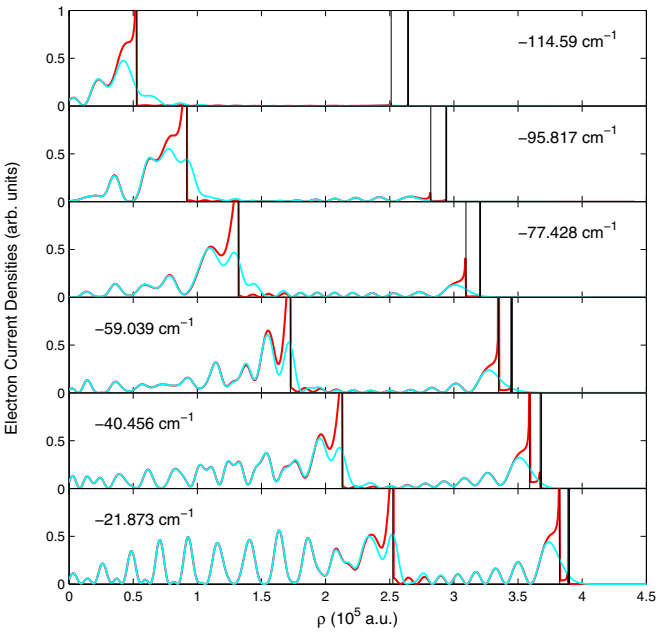

FIG. 3. Ejected electron current densities, due to photoionization of Li atoms in an electric field of 1000 V/cm, at six energies from -114.59 to -21.873 cm^{-1} away from any resonance. The detector is assumed to be located at $z_{\rm det} = -1000$ μm from the atomic source. The red curves represent the results from the generalized OOT, and the cyan curves indicate the divergent current densities fixed at caustics, denoted with the black vertical lines, using the uniform approximation.

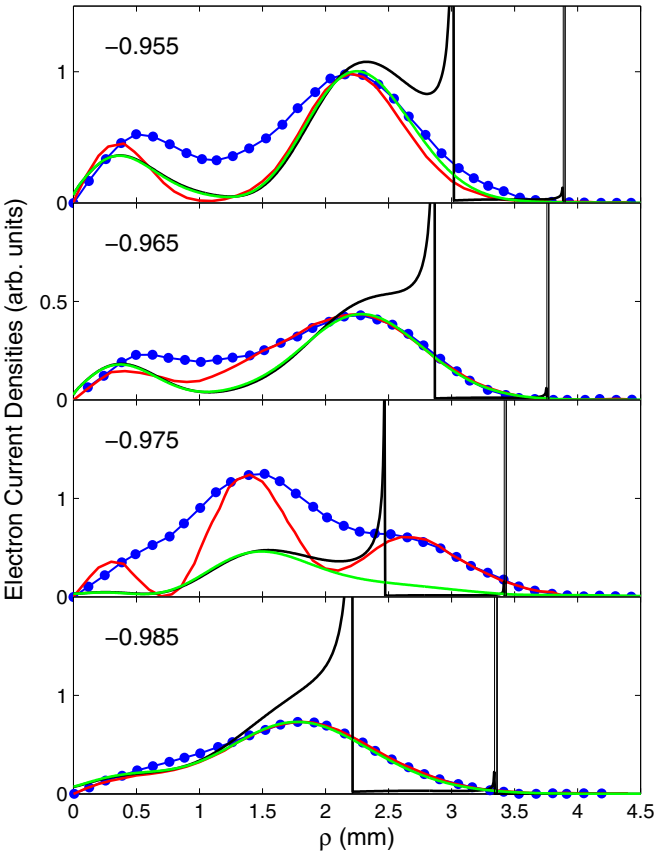

FIG. 5. Comparison among electron current densities from the generalized OOT, the wave-packet propagation technique, and the recent photoionization microscopy experiment for the four energies. The data listed in each panel are given by $\varepsilon = E/|E_{\rm sp}|$ using the value $\varepsilon = -0.975$, corresponding to the data of Cohen *et al.* [15]. The detector is assumed to be located at $z_{\rm det} = -1000$ μm from the atomic source. The blue dots and red curves represent the experimental electron current densities and those from the wave-packet propagation technique, while the black and green curves indicate current densities from the generalized OOT and uniform approximation, respectively. The black vertical lines denote caustics. Note: the experimental dots are connected with a smooth solid line to guide the eye.

with both experiment and the wave-packet propagation calculations in Fig. 5. One sees the diverged current densities denoted by the vertical lines. This is because semiclassical waves undergo refraction near a fold-type caustic surface dividing the configuration space into the classically allowed and forbidden regions, and therefore the semiclassical wave functions display singularities at the caustic surfaces. The theoretical method from the uniform approximation developed in Ref. [10] is able to fix such singularities. Here we adopt the uniform approximation to calculate the electron current densities of Li atoms. The obtained results from the uniform approximations are plotted together with those from the semiclassical OOT in this figure. It is apparent that the uniform and semiclassical approximations except for the divergence of the semiclassical currents at the caustics are in good agreement for each energy.

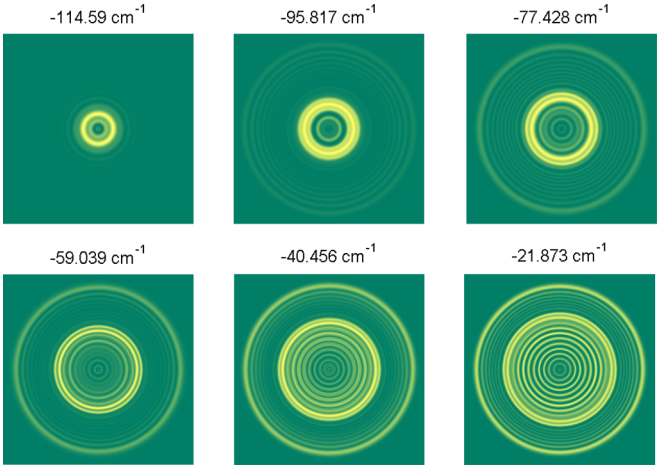

FIG. 4. Contour plots of electron current densities corresponding to Fig. 3 from the uniform approximation.

The electron current densities from experiment and theoretical calculations from the wave-packet propagation technique are also plotted in Fig. 5 for the purpose of comparison. Our theoretical calculations are found to be in agreement with the experimental and theoretical results for the three off-resonance energies, where the numbers of fringes are apparently reproduced well, but their relative intensities and contrasts are not. Even so, such an agreement is satisfactory in view of the limited experimental resolution. However, it is found that for the on-resonance energy -182.70 cm^{-1} denoted by $\varepsilon = -0.975$, our calculations from the generalized OOT severely deviate from both the experiment and

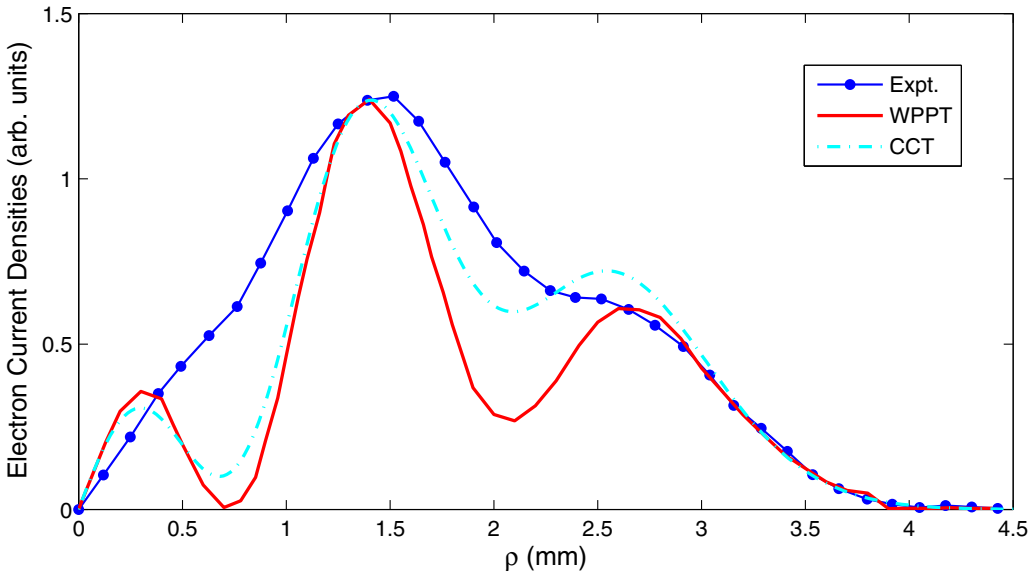

FIG. 6. Same as in Fig. 5, but for the $n_1^{\rm res} = 2$ resonance with $\varepsilon = -0.975$ as shown in the third panel of Fig. 5. The blue dots and red curves represent the experimental electron current densities (Expt.) and those from the wave packet propagation technique (WPPT), respectively. The cyan dashed curve are from the coupled-channel theory (CCT). Note: the experimental dots are connected with a smooth solid line to guide the eye.

theoretical results illustrated in Ref. [15]. The two nodes of the wave functions displayed in their experiment and theoretical calculations are not reproduced by our OOT. This is not surprising considering that semiclassical theory fails to describe tunneling through the potential barrier.

To explain the difference between experiment and theory for the on-resonance energy $-182.70\,{\rm cm}^{-1}$ shown in Ref. [15], we adopt the fully quantum-mechanical CCT developed in Ref. [23] to calculate the electron current densities at this on-resonance energy. The distribution of the electron current densities from the experimental measurements and theoretical calculations using the wave-packet propagation technique are compared in Fig. 6. The comparison shows satisfactory agreement. The two nodes of the wave functions have been clearly observed. However, the experimental relative intensities are not reproduced well. The difference may be attributed to the limited experimental resolution.

IV. SUMMARY AND CONCLUSION

We have generalized the semiclassical open-orbit theory (OOT), previously developed to study photoionization microscopy for hydrogenic atoms, to describe the propagation of outgoing electron waves to macroscopic distances from a nonhydrogenic atomic source. First of all, we divide the configuration space into the inner and outer regions, and then the inner region is further divided into the short-range interaction region and Coulomb region. The expression of field-free outgoing electron waves in the Coulomb region is derived within the framework of full quantum-mechanical theory. In the outer region, we assume that electron waves propagate from the Coulomb region to macroscopic distances following classical trajectories. The semiclassical wave functions are constructed from the obtained classical trajectories. Finally, the semiclassical and fully quantum-mechanical wave functions are joined in the surface dividing the configuration space into the inner and outer regions.

The generalized OOT has been applied to calculate spatial distributions of electron probability densities and current densities, produced due to photoionization for ground-state Li atoms in a uniform electric field of 1000 V/cm. The integrated probability densities are compared with those from the fully quantum-mechanical coupled-channel theory, and excellent agreement is found. The comparison confirms the reliability of the generalized OOT. Using the OOT, we investigated the contribution of ionization from direct and indirect trajectories to the interference patterns on a detector. Also the electron current densities are compared with the recent photoionization microscopy experiment and wave-packet propagation technique calculations. Satisfactory agreement has been seen with the wave-packet propagation technique calculations.

In summary, we developed a generalized open-orbit theory to describe the propagation of outgoing electron waves to macroscopic distances from a nonhydrogenic atom source. This theory is successful in predicting the spatial distributions of electron probability densities and current densities for Stark nonhydrogenic atoms for energies away from any resonance. Hopefully, it can be extended to calculate tunneling through the potential barrier in terms of the complex trajectory tunneling techniques as reported by Fabrikant and Gallup [27] and Schiff *et al.* [28]. This work is in progress.

ACKNOWLEDGMENTS

We thank Ilya I. Fabrikant for his helpful comments. This work was supported by the National Natural Science Foundation of China under Grant No. 11474079 (L.B.Z.) and the Postdoctoral Research Start-up Funds of Heilongjiang Province under Grant No. LBH-Q11013 (F.L.L.).

[1] F. Krausz and M. Ivanov, Rev. Mod. Phys. **81**, 163 (2009).
[2] J. Itatani, J. Levesque, D. Zeidler, H. Niikura, H. Pépin, J. C. Kieffer, P. B. Corkum, and D. M. Villeneuve, Nature (London) **432**, 867 (2004).
[3] D. Shafir, Y. Mairesse, D. M. Villeneuve, P. B. Corkum, and N. Dudovich, Nat. Phys. **5**, 412 (2009).
[4] C. Nicole, H. L. Offerhaus, M. J. J. Vrakking, F. Lépine, and C. Bordas, Phys. Rev. Lett. **88**, 133001 (2002).
[5] I. I. Fabrikant, Sov. Phys. JETP **52**, 1045 (1980).
[6] Yu. N. Demkov, V. D. Kondratovich, and V. N. Ostrovsky, Sov. Phys. JETP Lett. **34**, 403 (1981).
[7] V. D. Kondratovich and V. N. Ostrovsky, J. Phys. B **17**, 1981 (1984); **17**, 2011 (1984); **23**, 21 (1990); **23**, 3785 (1990).
[8] C. Nicole, I. Sluimer, F. Rosca-Pruna, M. Warntjes, M. J. J. Vrakking, C. Bordas, F. Texier, and F. Robicheaux, Phys. Rev. Lett. **85**, 4024 (2000).
[9] C. Bordas, F. Lépine, C. Nicole, and M. J. J. Vrakking, Phys. Rev. A **68**, 012709 (2003).
[10] L. B. Zhao and J. B. Delos, Phys. Rev. A **81**, 053417 (2010).
[11] L. B. Zhao and J. B. Delos, Phys. Rev. A **81**, 053418 (2010).
[12] S. Cohen, M. M. Harb, A. Ollagnier, F. Robicheaux, M. J. J. Vrakking, T. Barillot, F. Lépine, and C. Bordas, Phys. Rev. Lett. **110**, 183001 (2013).
[13] A. S. Stodolna, A. Rouzeé, F. Lépine, S. Cohen, F. Robicheaux, A. Gijsbertsen, J. H. Jungmann, C. Bordas, and M. J. J. Vrakking, Phys. Rev. Lett. **110**, 213001 (2013).
[14] L. B. Zhao, D. H. Xiao, and I. I. Fabrikant, Phys. Rev. A **91**, 043405 (2015).
[15] S. Cohen, M. M. Harb, A. Ollagnier, F. Robicheaux, M. J. J. Vrakking, T. Barillot, F. Lépine, and C. Bordas, Phys. Rev. A **94**, 013414 (2016).
[16] L. S. Rodberg and R. M. Thaler, *Introduction to the Quantum Theory of Scattering* (Academic, New York, 1967), p. 82.
[17] M. J. Seaton, Rep. Prog. Phys. **46**, 167 (1983).
[18] M. L. Du and J. B. Delos, Phys. Rev. A **38**, 1896 (1988); **38**, 1913 (1988).
[19] L. B. Zhao, I. I. Fabrikant, and M. L. Du, Phys. Rev. A **91**, 067402 (2015).
[20] J. Gao and J. B. Delos, Phys. Rev. A **46**, 1455 (1992).
[21] M. L. Du, Phys. Rev. A **40**, 4983 (1989).
[22] W. L. McMillian, Phys. Rev. A **4**, 69 (1971).
[23] L. B. Zhao, I. I. Fabrikant, J. B. Delos, F. Lépine, S. Cohen, and C. Bordas, Phys. Rev. A **85**, 053421 (2012).
[24] I. I. Fabrikant and L. B. Zhao, Phys. Rev. A **91**, 053412 (2015).
[25] J. Gao, J. B. Delos, and M. Baruch, Phys. Rev. A **46**, 1449 (1992).
[26] C. Bordas, Phys. Rev. A **58**, 400 (1998).
[27] I. I. Fabrikant and G. A. Gallup, Phys. Rev. A **79**, 013406 (2009).
[28] J. Schiff, Y. Goldfarb, and D. J. Tannor, Phys. Rev. A **83**, 012104 (2011).